JOURNAL OF COMPUTATIONAL PHYSICS 103, 126–140 (1992)

Radiation-Induced Cavitation Process in a Metastable Superheated Liquid

II. Interface Formation and Post-interface Formation Stages

Y. Y. SUN, B. T. CHU, AND R. E. APFEL

Department of Mechanical Engineering, Yale University, New Haven, Connecticut 06520

Received September 15, 1989; revised September 30, 1991

In Part I, the flow fields in the initial stage and the pre-bubble formation stage of the radiation-induced cavitation process in a metastable superheated liquid were solved by the scaling transformation and donor-cell treatment, respectively. In Part II, Miller's simple moving finite element method (simple MFEM) was used to compute the flow fields of the vapor–liquid interface formation stage and the post-interface formation stage for superheated isobutane and Freon-12. However, to be comprehensive, the MFEM in non-hierarchical p-refinement form was derived. The results, which are in fair agreement with the experimental data, give estimates of the threshold energies for cavitation, calculate the speeds of both the interface and the shock wave, determine the time scales and the length scales involved in the process. The results presented describe, for the first time, the detailed transformation occurring inside a superheated-droplet neutron detector. Results are immediately applicable to bubble chambers.

1. INTRODUCTION

The flow fields at the initial stage and pre-bubble formation stage were solved in Part I [14], using the scaling transformation and implicit donor-cell finite difference method (FDM). But the non-adaptive finite difference method cannot be expected to give satisfactory answers in describing the formation and growth of the vapor–liquid interface. Indeed, even prior to the first appearance of this interface, we have witnessed (part I) a steady increase (with time) of the density gradient in the medium. This steepening in density gradient is caused not so much by the usual nonlinear convection terms but by the behavior of the pv-curve at fluid temperatures slightly above the critical temperature. It occurs in anticipation of the phase change that will soon follow. Evidently some type of adaptive computational schemes [2, 3, 10–13, 15] must be used to describe the phenomenon.

There is another relevant point which should be made. In the initial and pre-bubble formation stages, shock propagation is determined principally by the energy deposition and is closely coupled to the process leading to formation of the vapor–liquid interface. It is for this reason that a scaling transformation in the radial coordinate is made to render the shock location fixed at $\bar{R} = 1$. However, after the bubble is formed, the propagation of the shock wave is largely governed by the growth or decay of the bubble. The length scale of interest is of the order of the radius of the bubble rather than the radius of the shock wave. It is evident that maintaining the scaling transformation used in the earlier pre-bubble formation stage would diminish the region of interest to an increasingly smaller size. This is obviously undesirable; therefore, the earlier scaling transformation must be abandoned and the location of the propagating shock front must be determined at each instant. Thus, in the radiation-induced cavitation problem, it is necessary to have an adaptive computational method which can easily deal with multiple moving steep gradients. After some consideration, we adopted Miller's simple moving finite element method (simple MFEM) [4, 7, 8] to compute the flow fields in the bubble formation and development stages. The solutions of the finite difference method in the pre-bubble formation stage will be used as the starting values of the MFEM. (The reasons why we did not connect the MFEM directly with the similarity solution have already been explained in the introduction of part I).

In this part, Miller's moving finite element method in general form will first be derived. The governing equations will be established in the variables convenient for describing the changes in the bubble formation stage and post-bubble formation stage. Next, the implementation of the MFEM will be discussed. Two media, i.e., isobutane and Freon-12, will be tested and the principal results exhibited.

2. MILLER'S MOVING FINITE ELEMENT METHOD

The MFEM moves the nodes into regions of steep gradients automatically and is especially useful in handling multiple moving steep gradients with far fewer nodes than would otherwise be the case. The non-hierarchical

0021-9991/92 $5.00

p-refinement MFEM will be derived in this section for the following two purposes: First, the piecewise linear approximation (Miller's scheme) is its simplest case; second, it will be used in our future work.

In this method, one considers a system of partial differential equations

$$\dot{\mathbf{u}} - \mathbf{L}(\mathbf{u}) = 0, \qquad t \geqslant 0, \tag{1}$$

where $\mathbf{u}$ and $\mathbf{L}$ are vector-valued functions, i.e., $\mathbf{u} = (u^1, u^2, ..., u^p)^T$, $\dot{\mathbf{u}}$ is the time derivative of $\mathbf{u}$ and $\mathbf{L} = (L^1, L^2, ..., L^p)^T$ is some partial differential operator, linear or nonlinear, in the xt-domain. If $\mathbf{u}$ is given at $t = 0$, then we can compute $\mathbf{u}(t)$ for $t > 0$. One can approximate the required solution by the functions

$$u^l = \sum_{i=1}^{n} a_i^l \alpha_i^{(1)} + w_i^l \alpha_i^{(2)} + v_i^l \alpha_i^{(3)}, \qquad l = 1, 2, ..., p, \tag{2}$$

where

$$\begin{aligned} \alpha_i^{(1)} &= \frac{x - s_{i-1}}{s_i - s_{i-1}}, && x \in [s_{i-1}, s_i), \\ &= \frac{s_{i+1} - x}{s_{i+1} - s_i}, && x \in [s_i, s_{i+1}), \\ &= 0, && \text{elsewhere,} \end{aligned} \tag{3a}$$

$$\begin{aligned} \alpha_i^{(2)} &= \frac{4}{(s_i - s_{i-1})^2}(x - s_{i-1})(s_i - x), && x \in [s_{i-1}, s_i), \\ &= \frac{4}{(s_{i+1} - s_i)^2}(x - s_i)(s_{i+1} - x), && x \in [s_i, s_{i+1}), \\ &= 0, && \text{elsewhere,} \end{aligned} \tag{3b}$$

$$\begin{aligned} \alpha_i^{(3)} &= -\frac{12\sqrt{3}}{(s_i - s_{i-1})^3}(x - s_{i-1})(s_i - x)(x - \tfrac{1}{2}(s_{i-1} + s_i)), \\ &\qquad x \in [s_{i-1}, s_i), \\ &= \frac{12\sqrt{3}}{(s_{i+1} - s_i)^3}(x - s_i)(s_{i+1} - x)(x - \tfrac{1}{2}(s_i + s_{i+1})), \\ &\qquad x \in [s_i, s_{i+1}), \\ &= 0, \qquad \text{elsewhere.} \end{aligned} \tag{3c}$$

In the above, $\alpha_i^{(1)}$, $\alpha_i^{(2)}$, and $\alpha_i^{(3)}$ are called the shape functions or the basis functions and are illustrated in Fig. 1.

Then, the solutions on the jth cell $[s_{j-1}, s_j]$ can be expressed as

$$\begin{aligned} u^l = \Bigg[& a_{j-1}^l + \frac{(a_j^l - a_{j-1}^l)}{(s_j - s_{j-1})}(x - s_{j-1}) + 4(w_{j-1}^l + w_j^l) \\ & \times \frac{(x - s_{j-1})(s_j - x)}{(s_j - s_{j-1})^2} + 12\sqrt{3}\,(v_{j-1}^l - v_j^l) \\ & \times \frac{(x - s_{j-1})(s_j - x)(x - \frac{1}{2}(s_j + s_{j-1}))}{(s_j - s_{j-1})^3} \Bigg], \\ & x \in [s_{j-1}, s_j). \end{aligned} \tag{4}$$

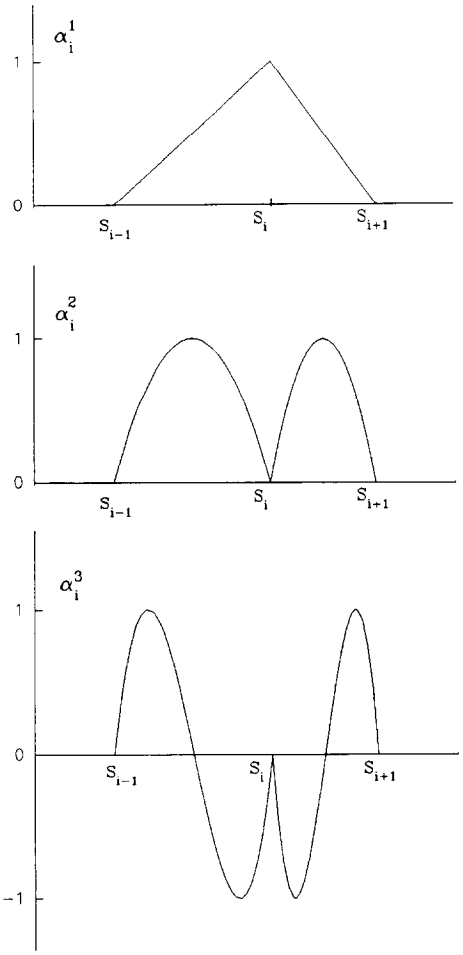

FIG. 1. Basis function of the non-hierarchical P-version MFEM.

Obviously, the solution u^l is a function of $a_i^l(t)$, $w_i^l(t)$, $v_i^l(t)$, and $s_i(t)$, $i = 1, ..., n$; $l = 1, ..., p$; i.e.,

$$\begin{aligned} u^l = u^l(a_1^l(t), ..., a_n^l(t), w_1^l(t), ..., w_n^l(t), v_1^l(t), ..., \\ v_n^l(t), s_1(t), ..., s_n(t)). \end{aligned} \tag{5}$$

The first derivative of u^l with respect to time t is given by

$$\dot{u}^l = \frac{du^l}{dt} = \sum_{i=1}^{n} \frac{\partial u^l}{\partial a_i^l}\dot{a}_i^l + \frac{\partial u^l}{\partial w_i^l}\dot{w}_i^l + \frac{\partial u^l}{\partial v_i^l}\dot{v}_i^l + \frac{\partial u^l}{\partial s_i}\dot{s}_i. \tag{6}$$

Defining

$$\begin{aligned} \alpha_i^{(1)} &= \frac{\partial u^l}{\partial a_i^l}, \\ \alpha_i^{(2)} &= \frac{\partial u^l}{\partial w_i^l}, \\ \alpha_i^{(3)} &= \frac{\partial u^l}{\partial v_i^l}, \\ \beta_i^l &= \frac{\partial u^l}{\partial s_i}, \end{aligned} \tag{7}$$

one thus finds

$$\dot{u}^l = \sum_{i=1}^{n} \alpha_i^{(1)} \dot{a}_i^l + \alpha_i^{(2)} \dot{w}_i^l + \alpha_i^{(3)} \dot{v}_i^l + \beta_i^l \dot{s}_i. \tag{8}$$

Here, $\alpha_i^{(1)}$, $\alpha_i^{(2)}$, and $\alpha_i^{(3)}$ are listed in Eq. (3), and β_i^l is given by

$$\begin{aligned}
\beta_i^l &= -m_i^l \alpha_i^{(1)} + 4(w_i^l + w_{i-1}^l) \frac{(x - s_{i-1})}{(s_i - s_{i-1})^2} - 8(w_i^l + w_{i-1}^l) \\
&\quad \times \frac{(x - s_{i-1})(s_i - x)}{(s_i - s_{i-1})^3} + 12\sqrt{3}\,(v_{i-1}^l - v_i^l) \\
&\quad \times \frac{(x - s_{i-1})[(x - \frac{1}{2}(s_i + s_{i-1})) - \frac{1}{2}(s_i - x)]}{(s_i - s_{i-1})^3} \\
&\quad - 36\sqrt{3}\,(v_{i-1}^l - v_i^l) \frac{(x - s_{i-1})(s_i - x)(x - \frac{1}{2}(s_i + s_{i-1}))}{(s_i - s_{i-1})^4}, \\
&\qquad x \in [s_{i-1}, s_i), \\
&= -m_{i+1}^l \alpha_i^{(1)} - 4(w_i^l + w_{i+1}^l) \frac{(s_{i+1} - x)}{(s_{i+1} - s_i)^2} + 8(w_i^l + w_{i+1}^l) \\
&\quad \times \frac{(x - s_i)(s_{i+1} - x)}{(s_{i+1} - s_i)^3} - 12\sqrt{3}\,(v_i^l - v_{i+1}^l) \\
&\quad \times \frac{(s_{i+1} - x)[(x - \frac{1}{2}(s_i + s_{i+1})) + \frac{1}{2}(x - s_i)]}{(s_{i+1} - s_i)^3} \\
&\quad + 36\sqrt{3}\,(v_i^l - v_{i+1}^l) \frac{(x - s_i)(s_{i+1} - x)(x - \frac{1}{2}(s_i + s_{i+1}))}{(s_{i+1} - s_i)^4}, \\
&\qquad x \in [s_i, s_{i+1}), \\
&= 0, \qquad \text{elsewhere.}
\end{aligned} \tag{9}$$

In the above,

$$\begin{aligned}
m_j^l &= \frac{a_j^l - a_{j-1}^l}{s_j - s_{j-1}}, \\
m_{j+1}^l &= \frac{a_{j+1}^l - a_j^l}{s_{j+1} - s_j}.
\end{aligned} \tag{10}$$

The residue $\mathbf{R}$ is defined as

$$\mathbf{R} = \dot{\mathbf{u}} - L(\mathbf{u}). \tag{11}$$

The values of a_j^l, w_j^l, v_j^l, and s_j are chosen in a least square sense, i.e.,

$$\begin{aligned}
\frac{\partial(\mathbf{R}, \mathbf{R})}{\partial \dot{a}_j^l} &= 0, \\
\frac{\partial(\mathbf{R}, \mathbf{R})}{\partial \dot{w}_j^l} &= 0, \\
\frac{\partial(\mathbf{R}, \mathbf{R})}{\partial \dot{v}_j^l} &= 0, \\
\frac{\partial(\mathbf{R}, \mathbf{R})}{\partial \dot{s}_j} &= 0.
\end{aligned} \tag{12}$$

The above equations can be written in matrix form,

$$\mathbf{A}(\mathbf{y})\,\dot{\mathbf{y}} = \mathbf{G}(\mathbf{y}), \tag{13}$$

where

$$\begin{aligned}
\mathbf{y} = (&a_1^1, ..., a_1^p, w_1^1, ..., w_1^p, v_1^1, ..., v_1^p, s_1, ..., a_n^1, ..., a_n^p, w_n^1, ..., \\
&w_n^p, v_n^1, ..., v_n^p, s_n)^{\mathrm{T}}
\end{aligned} \tag{14}$$

and

$$\mathbf{G} = (g_1, g_2, g_3, ..., g_{(n \times (3 \times p + 1))}) \tag{15}$$

are $n \times (3 \times p + 1)$-dimensional column vectors of the unknown parameters and $\mathbf{A}$ is the $(n \times (3 \times p + 1)) \times (n \times (3 \times p + 1))$ matrix,

$$\mathbf{A} = \begin{pmatrix}
A_1 & B_1 & & & & \\
C_2 & A_2 & B_2 & & 0 & \\
 & C_3 & A_3 & B_3 & & \\
 & & \ddots & \ddots & \ddots & \\
 & 0 & & C_{n-1} & A_{n-1} & B_{n-1} \\
 & & & & C_n & A_n
\end{pmatrix}. \tag{16}$$

Here,

$$\begin{aligned}
C_i &= D_{i,i-1} + \bar{D}_{i,i-1}, \\
A_i &= D_{i,i} + \bar{D}_{i,i}, \\
B_i &= D_{i,i+1} + \bar{D}_{i,i+1},
\end{aligned} \tag{17}$$

$$D_{i,j} = \begin{pmatrix}
E_{i,j} & & & & & T_{i,j}^1 \\
 & E_{i,j} & & & 0 & T_{i,j}^2 \\
 & & E_{i,j} & & & T_{i,j}^3 \\
 & & & \ddots & & \vdots \\
 & 0 & & & E_{i,j} & T_{i,j}^p \\
H_{i,j}^1 & H_{i,j}^2 & H_{i,j}^3 & \cdots & H_{i,j}^p & Q_{i,j}
\end{pmatrix}, \tag{18}$$

where

$$E_{i,j} = \begin{pmatrix}
(\alpha_i^{(1)}, \alpha_j^{(1)}) & (\alpha_i^{(1)}, \alpha_j^{(2)}) & (\alpha_i^{(1)}, \alpha_j^{(3)}) \\
(\alpha_i^{(2)}, \alpha_j^{(1)}) & (\alpha_i^{(2)}, \alpha_j^{(2)}) & (\alpha_i^{(2)}, \alpha_j^{(3)}) \\
(\alpha_i^{(3)}, \alpha_j^{(1)}) & (\alpha_i^{(3)}, \alpha_j^{(2)}) & (\alpha_i^{(3)}, \alpha_j^{(3)})
\end{pmatrix} \tag{19a}$$

$$T_{i,j}^l = ((\alpha_i^{(1)}, \beta_j^l), (\alpha_i^{(2)}, \beta_j^l), (\alpha_i^{(3)}, \beta_j^l))^{\mathrm{T}} \tag{19b}$$

$$H_{i,j}^l = ((\beta_i^l, \alpha_j^{(1)}), (\beta_i^l, \alpha_j^{(2)}), (\beta_i^l, \alpha_j^{(3)})), \tag{19c}$$

$$Q_{i,j} = \sum_{l=1}^{p} (\beta_i^l, \beta_j^l),$$

$$i = 1, 2, ..., n; \qquad j = 1, 2, ..., n, \tag{19d}$$

and $\bar{D}_{i,j}$ are $(3\times p+1)\times(3\times p+1)$ matrices, n is the total number of nodes. $\bar{D}_{i,j}$ is a zero matrix except when $j=i-1$, $j=i$, $j=i+1$, in which case the last element (i.e., the $(3\times p+1,\ 3\times p+1)$th element) has the value $d_{i,j}$, where $d_{i,i-1}=-e_i^2$ for $j=i-1$; $d_{i,i}=e_i^2+e_{i+1}^2$ for $j=i$; $d_{i,i+1}=-e_{i+1}^2$ for $j=i+1$, and e_i is defined in Eq. (21a) below. The right-hand side of Eq. (13), **G**, is a column vector of order $n\times(3\times p+1)$ whose elements are

$$\begin{aligned}
g_{(3p+1)i-3p}&=(\alpha_i^{(1)},\ L^1(\mathbf{u})),\\
g_{(3p+1)i-(3p-1)}&=(\alpha_i^{(2)},\ L^1(\mathbf{u})),\\
g_{(3p+1)i-(3p-2)}&=(\alpha_i^{(3)},\ L^1(\mathbf{u})),\\
&\vdots\\
g_{(3p+1)i-3}&=(\alpha_i^{(1)},\ L^p(\mathbf{u})),\\
g_{(3p+1)i-2}&=(\alpha_i^{(2)},\ L^p(\mathbf{u})),\\
g_{(3p+1)i-1}&=(\alpha_i^{(3)},\ L^p(\mathbf{u})),\\
g_{(3p+1)i}&=\sum_{l=1}^{p}(\beta_i^l,\ L^l(\mathbf{u}))+e_iF_i-e_{i+1}F_{i+1},\\
&\qquad i=1,\ 2,\ \ldots,\ n.
\end{aligned}\tag{20}$$

In the above,

$$e_i=\frac{k_2}{(s_i-s_{i-1})-k_1}+k_3,\tag{21a}$$

$$F_i=\frac{k_4}{(s_i-s_{i-1})-k_1},\qquad i=1,\ 2,\ \ldots,\ n,\tag{21b}$$

where k_1, k_2, k_3, and k_4 are small positive constants; e_i and F_i are called regularization terms introduced by Miller to prevent matrix **A** from becoming singular.

3. DIMENSIONLESS GOVERNING EQUATIONS AND BOUNDARY CONDITIONS

The simple MFEM, as a direct result of the above non-hierarchical p-refinement MFEM, is be applied in this section to solve the flow fields at large times, covering the last part of the pre-bubble formation stage, the interface-formation stage, and the bubble developing stage. Define

$$L=\left(\frac{\bar{E}}{\pi\rho_0R^*T_0}\right)^{1/2},$$

$$\bar{E}=2\pi\rho_0R^2\dot{R}^2\int_0^1 x\,dx(\bar{e}+\tfrac{1}{2}\bar{u}^2)/\bar{v},$$

$$u_g=(R^*T_0)^{1/2}$$

and introduce the dimensionless variables,

$$\tilde{u}=\frac{u}{u_g},\qquad \tilde{e}=\frac{e-e_0}{u_g^2},\qquad \tilde{p}=\frac{p}{\rho_0u_g^2},$$

$$\tilde{T}=\frac{T}{T_0},\qquad \tilde{\rho}=\frac{\rho}{\rho_0},\qquad \tilde{v}=\frac{v}{v_0},$$

$$\tilde{t}=\frac{u_gt}{L},\qquad \tilde{r}=\frac{r}{L},\qquad \tilde{f}_s=\frac{f}{u_g^2/L},$$

where f_s is the body force per unit mass. The related symbols were defined in part I except for the new symbols introduced in part II. The governing equations and the boundary conditions, i.e., Eqs. (1)–(5) in part I [14] become

$$\frac{\partial\tilde{v}}{\partial\tilde{t}}=\frac{\tilde{v}^2}{\tilde{r}}\frac{\partial}{\partial\tilde{r}}\left(\frac{\tilde{u}\tilde{r}}{\tilde{v}}\right),\tag{22}$$

$$\frac{\partial\tilde{u}}{\partial\tilde{t}}=\tilde{f}_s-\tilde{u}\frac{\partial\tilde{u}}{\partial\tilde{r}}+\frac{4}{3}\tilde{v}\tilde{\mu}\frac{\partial}{\partial\tilde{r}}\left[\frac{1}{\tilde{r}}\frac{\partial}{\partial\tilde{r}}(\tilde{u}\tilde{r})\right]+\frac{4}{3}\tilde{v}\frac{\partial\tilde{\mu}}{\partial\tilde{r}}\left[\frac{\partial\tilde{u}}{\partial\tilde{r}}-\frac{1}{2}\frac{\tilde{u}}{\tilde{r}}\right]-\tilde{v}\left(\tilde{p}_{\tilde{T}}\frac{\partial\tilde{T}}{\partial\tilde{r}}+\tilde{p}_{\tilde{v}}\frac{\partial\tilde{v}}{\partial\tilde{r}}\right),\tag{23}$$

and

$$\tilde{c}_{\tilde{v}}\left(\frac{\partial\tilde{T}}{\partial\tilde{t}}+\tilde{u}\frac{\partial\tilde{T}}{\partial\tilde{r}}\right)=-\frac{\tilde{v}\tilde{T}\tilde{p}_{\tilde{T}}}{\tilde{r}}\frac{\partial}{\partial\tilde{r}}(\tilde{u}\tilde{r})+\frac{4}{3}\tilde{\mu}\tilde{v}\left[\frac{1}{\tilde{r}}\frac{\partial}{\partial\tilde{r}}(\tilde{u}\tilde{r})\right]^2-4\tilde{\mu}\frac{\tilde{u}\tilde{v}}{\tilde{r}}\frac{\partial\tilde{u}}{\partial\tilde{r}}+\frac{\tilde{v}}{\tilde{r}}\frac{\partial}{\partial\tilde{r}}\left(\tilde{\kappa}\tilde{r}\frac{\partial\tilde{T}}{\partial\tilde{r}}\right),\tag{24}$$

where $\tilde{p}_{\tilde{T}}$ and $\tilde{p}_{\tilde{v}}$ are the partial derivatives of $\tilde{p}$ with respect to $\tilde{T}$ and $\tilde{v}$, and

$$\tilde{\mu}=\mu\Big/\left(\frac{E\rho_0}{\pi}\right)^{1/2},$$

$$\tilde{\kappa}=\frac{\kappa}{\rho R^*}\left(\frac{E}{\pi\rho_0}\right)^{-1/2},$$

$$\tilde{c}_{\tilde{v}}=\frac{c_v}{R^*},$$

$$\frac{\partial\tilde{p}}{\partial\tilde{T}}=\frac{T_0}{\rho_0u_g^2}\frac{\partial p}{\partial T}.$$

Horvath–Lin's equation of state [5] and the specific internal energy equation associated with the equation of state are

$$\tilde{p}=\frac{\tilde{T}}{\tilde{v}-\beta_h}-\frac{\alpha_h}{\tilde{T}\tilde{v}(\tilde{v}+\gamma_h)}\tag{25}$$

and

$$\tilde{e}=\int_1^{\tilde{T}} \tilde{c}_{\tilde{v}}(\tilde{T})\,d\tilde{T}+\frac{2\alpha_h}{\gamma_h\tilde{T}}\ln\left(\frac{\tilde{v}}{\tilde{v}+\gamma_h}\right)-\frac{2\alpha_h}{\gamma_h}\ln\left(\frac{1}{1+\gamma_h}\right), \tag{26}$$

where

$$\alpha_h=\frac{\alpha}{z_c}\left(\frac{v_c}{v_0}\right)\left(\frac{T_c}{T_0}\right)^2, \qquad \beta_h=\frac{\beta}{z_c}\left(\frac{v_c}{v_0}\right),$$

$$\gamma_h=\gamma\beta_h, \qquad z_c=\frac{p_c v_c}{R^* T_c}.$$

Here α, β, and γ are the parameters in Horvath–Lin's equation. The partial derivatives, $\tilde{p}_{\tilde{T}}$ and $\tilde{p}_{\tilde{v}}$ are given by

$$\tilde{p}_{\tilde{T}}=\frac{1}{\tilde{v}-\beta_h}+\frac{\alpha_h}{\tilde{T}^2\tilde{v}(\tilde{v}+\gamma_h)},$$

$$\tilde{p}_{\tilde{v}}=\frac{-\tilde{T}}{(\tilde{v}-\beta_h)^2}+\frac{\alpha_h}{\tilde{T}}\left[\frac{(\tilde{v}+\gamma_h)+\tilde{v}}{\tilde{v}^2(\tilde{v}+\gamma_h)^2}\right].$$

The boundary conditions at $\tilde{r}=0$ are

$$\begin{aligned}&\tilde{u}=0,\\ &\frac{\partial\tilde{T}}{\partial\tilde{r}}=0,\\ &\frac{\partial\tilde{p}}{\partial\tilde{r}}=\frac{4}{3}\tilde{\mu}\frac{\partial}{\partial\tilde{r}}\left[\frac{1}{\tilde{r}}\frac{\partial}{\partial\tilde{r}}(\tilde{u}\tilde{r})\right].\end{aligned} \tag{27a}$$

The third equation of Eqs. (27a) is derived from the momentum conservation equation, and also can be written in the non-conservation form with condition $\tilde{u}=0$ as $\tilde{r}\to 0$,

$$\frac{\partial\tilde{v}}{\partial\tilde{r}}=2\frac{\tilde{\mu}}{\tilde{p}_{\tilde{v}}}\frac{\partial^2\tilde{u}}{\partial\tilde{r}^2}. \tag{27b}$$

The boundary conditions as $\tilde{r}\to\infty$ are

$$\tilde{u}=0, \qquad \tilde{T}=1, \qquad \tilde{v}=1. \tag{28}$$

4. IMPLEMENTATION OF THE MFEM

4.1. *Operator*

Applying the simple MFEM to the governing equations (22), (23), and (24), written here in the form

$$U=(\tilde{v},\tilde{u},\tilde{T})^{\mathrm{T}}, \tag{29}$$

$$\dot{U}=\left(\frac{\partial\tilde{v}}{\partial\tilde{t}},\frac{\partial\tilde{u}}{\partial\tilde{t}},\frac{\partial\tilde{T}}{\partial\tilde{t}}\right)^{\mathrm{T}}, \tag{30}$$

$$L^1(U)=\frac{\tilde{v}^2}{\tilde{r}}\frac{\partial}{\partial\tilde{r}}\left(\frac{\tilde{u}\tilde{r}}{\tilde{v}}\right), \tag{31a}$$

$$L^2(U)=\tilde{f}_s-\tilde{u}\frac{\partial\tilde{u}}{\partial\tilde{r}}+\frac{4}{3}\tilde{v}\tilde{\mu}\frac{\partial}{\partial\tilde{r}}\left[\frac{1}{\tilde{r}}\frac{\partial}{\partial\tilde{r}}(\tilde{u}\tilde{r})\right]+\frac{4}{3}\tilde{v}\frac{\partial\tilde{\mu}}{\partial\tilde{r}}\left[\frac{\partial\tilde{u}}{\partial\tilde{r}}-\frac{1}{2}\frac{\tilde{u}}{\tilde{r}}\right]-\tilde{v}\frac{\partial\tilde{p}}{\partial\tilde{r}}, \tag{31b}$$

$$\tilde{c}_{\tilde{v}}L^3(U)=-\tilde{c}_{\tilde{v}}\tilde{u}\frac{\partial\tilde{T}}{\partial\tilde{r}}-\frac{\tilde{v}\tilde{T}\tilde{p}_{\tilde{T}}}{\tilde{r}}\frac{\partial}{\partial\tilde{r}}(\tilde{u}\tilde{r})+\frac{4}{3}\tilde{\mu}\tilde{v}\left[\frac{1}{\tilde{r}}\frac{\partial}{\partial\tilde{r}}(\tilde{u}\tilde{r})\right]^2-4\tilde{\mu}\frac{\tilde{u}\tilde{v}}{\tilde{r}}\frac{\partial\tilde{u}}{\partial\tilde{r}}+\frac{\tilde{v}}{\tilde{r}}\frac{\partial}{\partial\tilde{r}}\left(\tilde{\kappa}\tilde{r}\frac{\partial\tilde{T}}{\partial\tilde{r}}\right), \tag{31c}$$

we obtain a system of ordinary differential equations in the form of Eq. (13), where the $\mathbf{A}(\mathbf{y})$ is nearly singular. Equation (13) is, therefore, a stiff ODE system and care must be exercised in constructing its solution.

4.2. *Implicit Backward Euler Stiff ODE Solver*

Backward Euler and Newton iteration formulae. The implicit backward Euler formula (IBE) is chosen to solve Eq. (13),

$$\mathbf{A}_{n+1}(\mathbf{y}_{n+1}-\mathbf{y}_n)=h\cdot\mathbf{G}_{n+1}, \tag{32}$$

where h is the time increment Δt, subscripts n and $n+1$ signify values evaluated at the nth and $(n+1)$th time steps. The damped Newton iteration method is used to solve the above nonlinear algebraic system for $\mathbf{y}_{n+1}$,

$$\mathbf{y}_{n+1}^{[s+1]}=\mathbf{y}_{n+1}^{[s]}-(\mathbf{F}'^{[s]}_{n+1})^{-1}\cdot\mathbf{F}^{[s]}_{n+1}, \tag{33}$$

where

$$\mathbf{F}^{[s]}_{n+1}=\mathbf{A}^{[s]}_{n+1}(\mathbf{y}^{[s]}_{n+1}-\mathbf{y}_n)-h\mathbf{G}^{[s]}_{n+1} \tag{34}$$

and

$$\mathbf{F}'^{[s]}_{n+1}=\frac{\partial\mathbf{F}^{[s]}_{n+1}}{\partial\mathbf{y}^{[s]}_{n+1}}=\left[\mathbf{A}^{[s]}_{n+1}+\frac{\partial\mathbf{A}^{[s]}_{n+1}}{\partial\mathbf{y}^{[s]}_{n+1}}(\mathbf{y}^{[s]}_{n+1}-\mathbf{y}_n)-h\frac{\partial\mathbf{G}^{[s]}_{n+1}}{\partial\mathbf{y}^{[s]}_{n+1}}\right]. \tag{35}$$

In the above, $\mathbf{F}'^{[s]}_{n+1}$ is the Jacobian, $\mathbf{y}^{[s]}_{n+1}$ is the value of $\mathbf{y}_{n+1}$ obtained after s iterations, and $\mathbf{A}^{[s]}_{n+1}$ and $\mathbf{G}^{[s]}_{n+1}$ are $\mathbf{A}$ and $\mathbf{G}$ evaluated by $\mathbf{y}^{[s]}_{n+1}$. The starting value of iteration, denoted by $\mathbf{y}^{[0]}_{n+1}$, is obtained by solving the explicit linear algebraic system.

Jacobian. The Jacobian can be given by Eq. (35) in an analytic form or by a numerical difference scheme,

$$J_{i,j}=\frac{F_i(u_j+\Delta u_j)-F_i(u_j)}{\Delta u_j}. \tag{36}$$

The analytical form is used in this paper for better accuracy. We find that more than 80% of the total work is in calculating the Jacobian F' and its inverse for both the discretization process and the CPU times. The process of constructing the Jacobian in analytic form is illustrated in Appendix A.

IBE ODE solver. The IBE ODE solver is constructed by combining the implicit backward Euler formula and the Newton iteration method described above. The related error analysis is illustrated as follows.

The truncation error E_t of the IBE ODE solver is determined by Milne's device [6]:

$$E_t = \tfrac{1}{2}(y_{n+k}^{[s]} - y_{n+k}^{[0]}). \tag{37}$$

From the truncation error analysis, one can find that

$$y(x_{n+k}) - y_{n+k}^{[s]} = E_t + O(h^{p+2}), \tag{38}$$

where $y(x_{n+k})$ is the exact solution, $y_{n+k}^{[s]}$ is sth iteration solution, and p is the error order of a given difference operator (cf. p. 23 in [6]). The local truncation error of E_t is of the order of h^{p+1} (cf. p. 48 of [6]). Therefore, the relative error E_{rel} can be expressed as

$$E_{\text{rel}} = \frac{E_t}{y_{n+k}^{[s]} + E_t}. \tag{39}$$

Taking into consideration the A-stability of the IBE ODE solver, one can determine the time step length by the following error control requirements: (a) the truncation error $E_t \leqslant \varepsilon_t$, (b) the relative error $E_{\text{rel}} \leqslant \varepsilon_{\text{rel}}$, (c) the residue of Newton iteration $E_n = resi = \|\mathbf{F}\|_2$, $E_n \leqslant \varepsilon_n$, where ε_t, ε_{rel}, and ε_n are the given tolerances. The following tolerances are used: $\varepsilon_n = 10^{-3}$ except at beginning of the developing stage for which $\varepsilon_n = 10^{-4}$, $\varepsilon_{\text{rel}} = 10^{-3}$, and $\varepsilon_t = 10^{-3}$. The time step length h is always less than 10^{-3} if $\varepsilon_n = 10^{-3}$ and $\varepsilon_{\text{rel}} = 10^{-3}$ are used. For the implicity backward Euler formula, the local truncation error has the order of h^2. Thus, E_t is always less than 10^{-6}.

4.3. *Boundary Conditions*

Taking into consideration the boundary conditions Eqs. (27) (here using u instead of $\tilde{u}$, etc., for simplicity), one finds that

$$\begin{aligned} u_1 &= 0, \\ T_1 &= T_2, \\ v_2 - v_1 &= f(s_2, s_3, u_2, u_3, T_2, T_3), \end{aligned} \tag{40}$$

where the form of f depends on the manner by which Eqs. (27) is approximated.

The first derivatives of u_1, T_1, and $v_2 - v_1$ with respect to time t become

$$\begin{aligned} \dot{u}_1 &= 0, \\ \dot{T}_1 &= \dot{T}_2, \\ \dot{v}_2 - \dot{v}_1 &= \varphi(\dot{s}_2, \dot{s}_3, \dot{u}_2, \dot{u}_3, \dot{T}_2, \dot{T}_3; s_2, s_3, u_2, u_3, T_2, T_3). \end{aligned} \tag{41}$$

The matrix A and the Jacobian F' will be revised due to the contribution of boundary conditions.

On the other hand, we use a sufficiently large value of x_e to replace the boundary condition of mathematical infinity. The numerical results show that there is no notable difference in the solutions for $x_e = 5\tilde{R}_{\text{shock}}$ and $x_e = 2\tilde{R}_{\text{shock}}$. Therefore, we can fix a sufficiently large value of x_e, say, $x_e = 5\tilde{R}_{\text{shock}}$ for the whole calculation.

4.4. *Regularization Parameters and Node Number*

The regularization parameters k's can be divided into two types. One is k_1 and the other is k_2, k_3, and k_4. k_1 represents the minimum separation of two neighboring nodes and is simply assigned a value which would accurately resolve the critical physical processes. The values of k_2, k_3, and k_4 prevent the system from becoming unpredictably stiff and yield efficient numerical solutions. A number of different arguments yield the following Miller's suggestion to select the k's [8]

$$e_i \sim \frac{A^2}{\Delta s_i}, \tag{a}$$

$$e_i F_i \sim \frac{B^2}{(\Delta s_i)^2}, \tag{b}$$

$$B^2 \sim \nu\eta^2, \tag{c}$$

$$e_i = \frac{k_2}{\Delta s_i - k_1} + k_3, \tag{d}$$

$$F_i = \frac{k_4}{\Delta s_i - k_1}. \tag{e}$$

In Eqs. (a)–(e), η is the tolerance of the truncation error, ν is the coefficient of the diffusion term, and A is considerably larger than η for the sake of smoother regularization of the nodal movement; $\Delta s_i = s_i - s_{i-1}$, s_i is the nodal position. For the radiation-induced cavitation process, we assume the minimum separation of nodes $k_1 = 10^{-4}$, $\eta = 10^{-3}$, and $A = 10^{-2}$, and $\Delta s_i \sim k_1$ and $(\Delta s_i - k_1) \sim k_1$. The coefficient of diffusion term T_{xx} is about 10^{-1}. From Eqs. (a) and (d), we obtain $k_2 = 10^{-4}$, supposing $k_3 = 0$. From Eqs. (b), (c), and (e), we find $k_4 = 10^{-3}$. Miller [4] indicates that the calculation will be accelerated if the larger k_2 and k_4 are used. Our calculations of Burger's equation reach the same

conclusion. We tried $k_2 = 10^{-4}$–10^{-2} for the radiation-induced cavitation process and found that there is no notable difference between the solutions. Therefore, we selected $k_2 = 10^{-2}$ for efficiency.

In summary, in case of isobutane and Freon-12, the following regularization parameters are selected: $k_1 = 0.0001$, $k_2 = 0.01$, $k_3 = 0.0$, and $k_4 = 0.001$. The node number is 14. Generally speaking, the solutions are not sensitive to the regularization parameters if the k's are selected within certain regions by some estimations [8].

4.5. *Treatment of Discontinuous Quantities*

In the above equations, some parameters such as the viscous coefficient μ, the specific heat capacity c_v, and the thermal conductivity κ undergo an abrupt change once the bubble is formed, due to the existence of two distinctive regions, i.e., the vapor region and the liquid region. Furthermore, once the bubble is formed, the surface tension of the bubble will also be presented. The surface tension behaves like a δ-function centered at the point x_i. The mathematical treatment of the above discontinuous quantities will be discussed in this section.

Surface tension. The difference in pressure across a cylindrical interface (Fig. 2) is

$$\Delta p = \frac{\sigma(T)}{R}, \tag{42}$$

where R is the radius of the interface and $\sigma(T)$ is the surface tension at a temperature T. This relationship can be easily derived by considering a momentum balance across the interface, assuming that the interface propagates at a low Mach number. This pressure change can be accounted for by postulating a body force distribution given by $\tilde{f}_r \bar{e}_r$, where $\bar{e}_r$ is a unit vector in the radial direction and $\tilde{f}_r$ is the dimensionless body force,

$$\tilde{f}_r = -\frac{1}{\rho u_g^2}\frac{\sigma(T)}{x_R}\frac{\delta(x - x_R)}{L}, \tag{43}$$

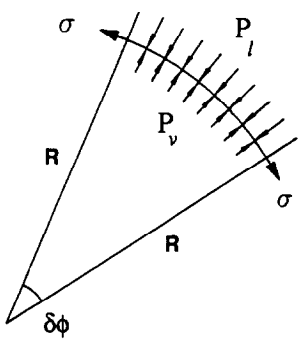

FIG. 2. Surface tension.

where $x_R = R/L$ is the dimensionless bubble radius and $x = r/L$ is the dimensionless radial distance, where L is the characteristic length, $\delta(x - x_R)$ is a one-dimensional delta function.

The surface tension σ as a function of temperature T can be described by [9]

$$\sigma = ([p]\,\rho_{lb})^4 \left(\frac{1 - T_r}{1 - T_{br}}\right)^{4n}, \tag{44}$$

where $[p]$ is a parameter related to the components of a given liquid and determined by experimental data; ρ_{lb} is the liquid density at the boiling temperature T_b. The reduced temperatures T_r and T_{br} are $T_r = T/T_c$ and $T_{br} = T_b/T_c$, respectively. The parameter n is given by experiments. Finally, the dimensionless quantity $\tilde{f}_r$ can be expressed by

$$\tilde{f}_r = -\frac{\alpha_p}{x_R u_g^2 \rho}\left(\frac{1 - \tilde{T}/\tilde{T}_c}{\alpha_T}\right)^{4n}\frac{\delta(x - x_R)}{L}, \tag{45}$$

where

$$\begin{aligned} &\alpha_p = ([p]\,\rho_{lb})^4, \qquad && \alpha_T = (1 - T_{br}), \\ &\tilde{T}_r = \frac{T}{T_0}, && \tilde{T}_c = \frac{T_c}{T_0}. \end{aligned} \tag{46}$$

Introducing the above into the right side of the momentum equation, i.e., Eq. (23); with the understanding that $\tilde{f}_r$ is zero unless the density gradient is sufficiently large, the governing equations can again be recast in the form shown in Eq. (13). For example, the term on the right-hand side of Eq. (20) can be calculated as

$$\begin{aligned} (\alpha_i, L^u(u)) &= \int_{s_{i-1}}^{s_{i+1}} \alpha_i \tilde{f}_r \, dx \\ &= \int_{s_{i-1}}^{s_i} \frac{(x - s_{i-1})}{(s_i - s_{i-1})}\tilde{f}_r \, dx + \int_{s_i}^{s_{i+1}} \frac{(s_{i+1} - x)}{(s_{i+1} - s_i)}\tilde{f}_r \, dx \\ &= \frac{(x_R - s_{i-1})}{(s_i - s_{i-1})}\frac{f_r^*}{L}, \qquad x_R \in (s_{i-1}, s_i) \\ &= \frac{f_r^*}{L}, \qquad x_R = s_i \\ &= \frac{(s_{i+1} - x_R)}{(s_{i+1} - s_i)}\frac{f_r^*}{L}, \qquad x_R \in (s_i, s_{i+1}), \end{aligned} \tag{47}$$

where

$$f_r^* = -\frac{\alpha_p}{x_R u_g^2 \rho}\left(\frac{1 - \tilde{T}/\tilde{T}_c}{\alpha_T}\right)^{4n}, \tag{48}$$

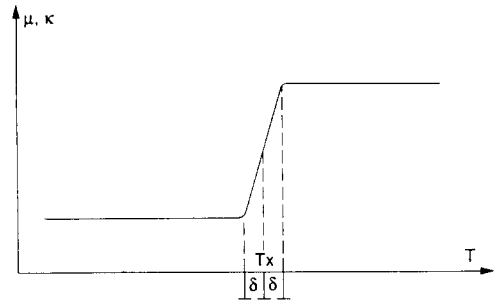

FIG. 3. Property function.

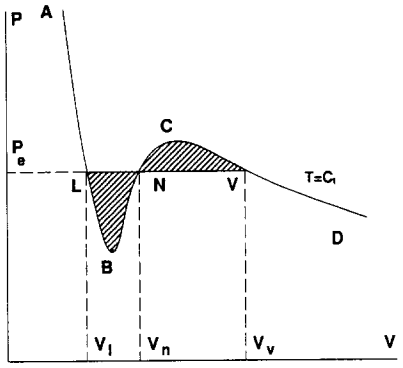

FIG. 4. Phase equilibrium for the superheated state.

and x_R is the position of that node when the density gradient has exceeded a critical value, arbitrarily chosen to be 15.

Discontinuity of medium properties. The following functions are introduced to describe the discontinuities of the viscous coefficient and the thermal conductivity such as

$$\tilde{\mu}(\tilde{T}) = \left[\frac{\lambda_\mu + 1}{2} - \frac{\lambda_\mu - 1}{\pi}\tan^{-1}\left(\frac{\tilde{T} - \tilde{T}_w}{\delta}\right)\right]\tilde{\mu}_{\text{vapor}},$$
$$\tilde{\kappa}(\tilde{T}) = \left[\frac{\lambda_\kappa + 1}{2} - \frac{\lambda_\kappa - 1}{\pi}\tan^{-1}\left(\frac{\tilde{T} - \tilde{T}_w}{\delta}\right)\right]\tilde{\kappa}_{\text{vapor}}, \tag{49}$$

where

$$\lambda_\mu = \frac{\tilde{\mu}_l}{\tilde{\mu}_v}, \qquad \lambda_c = \frac{\tilde{c}_{v,l}}{\tilde{c}_{v,v}}, \qquad \lambda_\kappa = \frac{\tilde{\kappa}_l}{\tilde{\kappa}_v}. \tag{50}$$

The subscripts l and v represent liquid and vapor, respectively. $\tilde{T}_w$ is the dimensionless temperature at the bubble wall and δ is a small number, e.g., 10^{-4}. In the above, we assume that the viscous coefficients and the thermal conductivities (also the special heat capacities) of both liquid and vapor are constants. The property function defined by Eqs. (49) is illustrated in Fig. 3. The specific heat capacity can be treated in a similar way.

Equation of state. A typical isotherm in the pv-diagram for Horvath–Lin's fluid is shown in Fig. 4. It is well known that the pressure at which the vapor phase is in equilibrium with the liquid phase is given by Maxwell's area rule. That is, at the equilibrium pressure p_e, the two shaded areas LBN and NCV are equal. This condition allows one to determine the vapor pressure $p_e(T)$ as a function of temperature T. This is shown in Fig. 5. The vapor–liquid coexistent line in the pv-diagram is shown in Fig. 6.

5. TESTING MEDIA

Isobutane and Freon-12 are used as the testing media. Their properties and relating data are listed in Tables I and II.

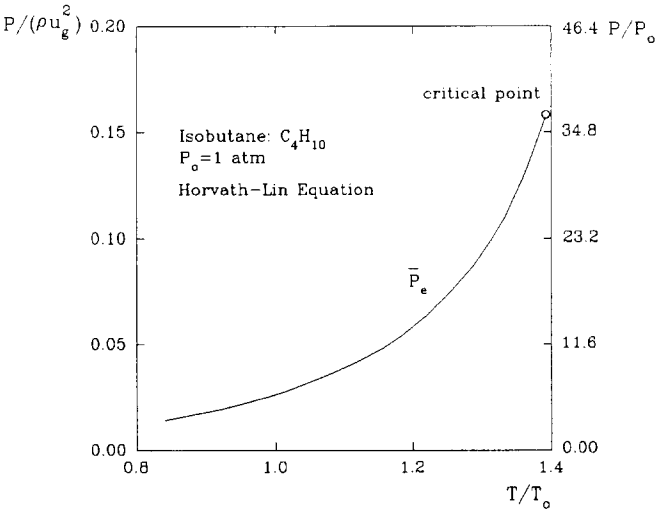

FIG. 5. Phase-equilibrium relation ($\bar{P} - \bar{T}$).

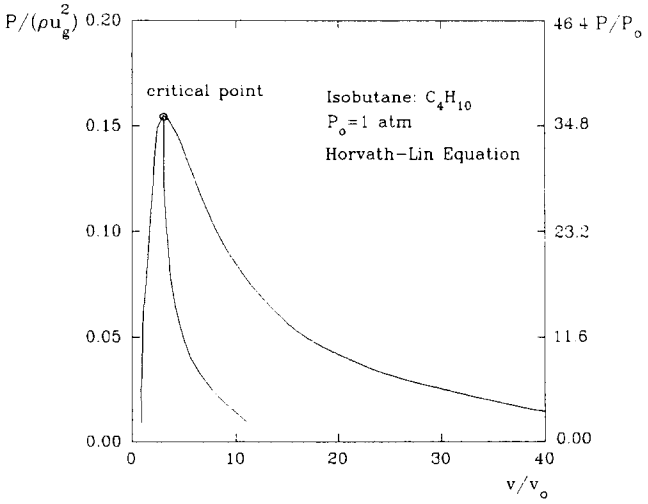

FIG. 6. $\bar{V}_1$, $\bar{V}_n$, and $\bar{V}_v$ via phase-equilibrium.

TABLE I

Parameters of Testing Media

Medium (chemical formula)	Isobutane (C_4H_{10})	Freon-12 ($C(CL)_2F_2$)
dE/dx(MeV · cm²/g)	6.98	1.28
$E_{neutron}$ (MeV)	1.55	0.20
$\bar{E}$ (g · cm/s²)	6.2318×10^{-3}	2.7263×10^{-3}
R_c (cm)(experiment)	1.186×10^{-5}	4.083×10^{-6}
L (cm) $E = E_c$	0.29132×10^{-5}	1.2475×10^{-6}
a (ergs · cm² °K/g²)	1.63379×10^{12}	1.23043×10^{12}
b (cm²/g)	1.35930	1.13214
c (cm²/g)	1.46077	1.27942
ϕ_0	0.0043349	0.0018170
$T_{boiling}$ (°K)	261.3	243.4
$[p]$	191.0	171.6
n	0.29	0.31

6. RESULTS AND DISCUSSIONS

The results calculated by the MFEM will be presented and compared with the experimental results in this section. The relating analyses will be given.

6.1. *Flow Fields*

Density distribution. Figures 7a, b, c, and d give the density distribution of isobutane with input energy $\bar{E} = 1.0\bar{E}_c$ at the initial temperature $T_0 = 20°C$, where $\bar{E}_c$ is the threshold energy determined by experiments. Quantitatively, it is equal to the stopping power dE/dx, i.e., $\bar{E}_c = dE/dx$. Figure 7a is a reproduction of the density distributions in the initial and pre-bubble formation stage given earlier (Fig. 12 in part I) with time relabeled in terms of $\bar{t}$. Figure 7a

TABLE II

Property Data of Testing Media

Medium (chemical formula)	Isobutane (C_4H_{10})	Freon-12 ($C(CL)_2F_2$)
ρ_0 (g/cm³)	0.55707	1.3290
T_0 (°C)	20	20
p_0 (atm)	1.00	1.00
T_c (°K)	408.1	385.0
v_c (cm³/g)	4.5248	1.7946
p_c (atm)	36.0	40.7
R^* (ergs/°K − g)	0.1431×10^7	0.6879×10^6
$(c_v)_{vapor}$ (cal/(g · mol − °K))	26.6672	17.1209
$(c_v)_{liquid}$ (cal/(g · mol − °K))	29.7476	24.3030
$(\eta)_{vapor}$ ($\mu p^b = 10^{-6}$(dynes/cm²))	90.30	167.102
$(\eta)_{liquid}$ ($cp^b = 10^{-2}$(dynes/cm²))	0.1535	0.1821
κ_{vapor} (μcal/cm · s · °K)	62.3067	22.4400
κ_{liquid} (μcal/cm · s · °K)	306.030	193.460
M (molecule weight)	58.124	120.914

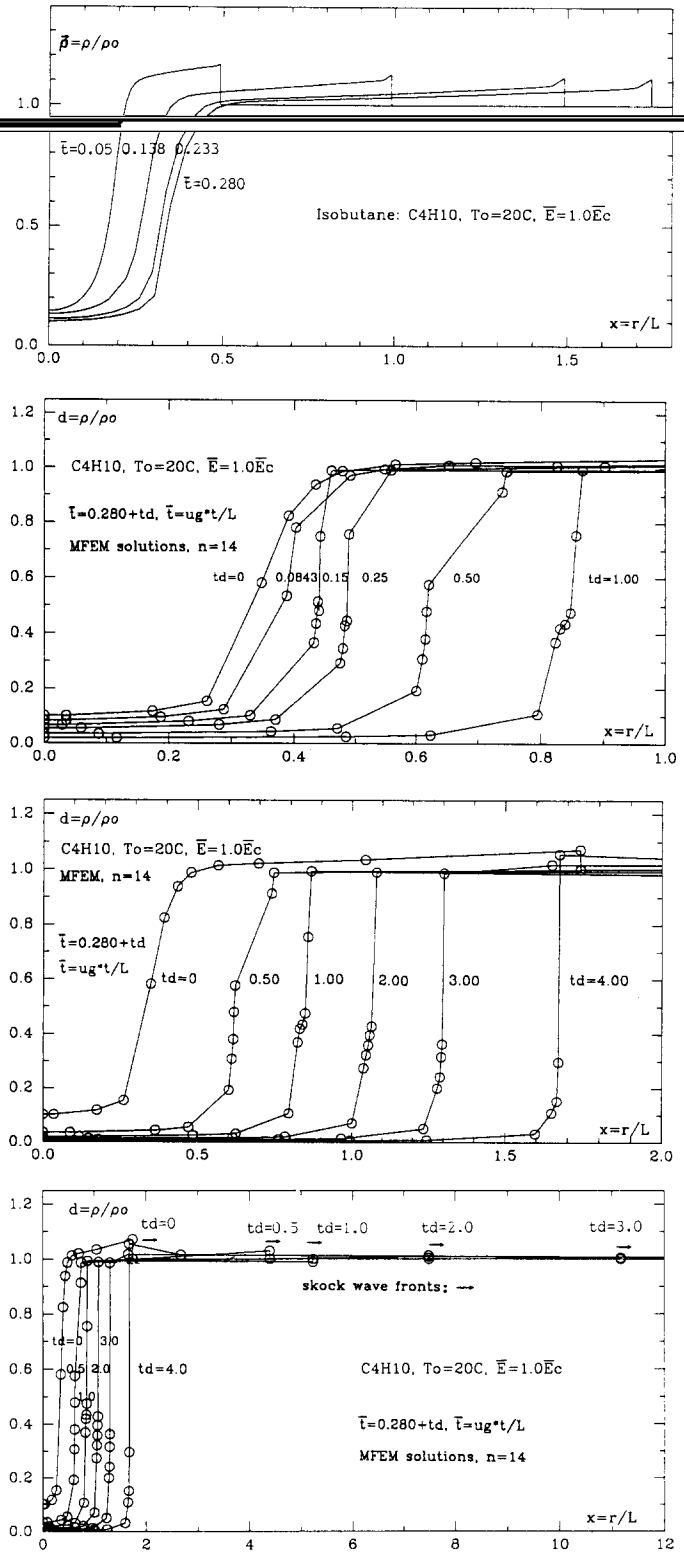

FIG. 7. (a) Normalized density distributions in the pre-bubble formation stage. $\bar{t} = 0.050$, 0.138, 0.233, and 0.280 are equivalent to $\bar{R} = 0.49$, 0.99, 1.49, and 1.74, respectively. (b) Normalized density distributions in the interface formation and developing stages from $td = 0$ to $td = 1.00$. (c) Normalized density distributions from $td = 0$ to $td = 4.00$. (d) Normalized density distributions and shock waves from $td = 0$ to $td = 4.00$.

shows how the density fields change from the beginning stage to a certain instant preceding the formation of a vapor–liquid interface, say, $\tilde{t} = 0.280$. The flow field at this instant will be used as the starting values of the MFEM. Figure 7b gives the density distributions computed by the MFEM from $\tilde{t} = 0.280$–1.0 within the space region $x = r/L \leqslant 1.0$, or equivalently, $td = 0$–1.0, where $\tilde{t} = 0.280 + td$. Figure 7c gives the density distributions from $td = 0$–4.0 within the space region $x = r/L \leqslant 2.0$ and Fig. 7d illustrates the density fields from $td = 0$–4.0 within the space region $x \leqslant 12.0$.

Figure 7c shows that the density gradient becomes steeper and steeper with time evolution. In the calculation, the surface tension is introduced if $d\tilde{\rho}/d\tilde{x} \geqslant 15.0$. This requirement means that the vapor wall thickness $\tilde{d}_w \leqslant 0.066$, i.e., $d_w = \tilde{d}_w \cdot L = 19.2 \times 10^{-8}$ cm $= 19.2$ Å. In Fig. 7b, one can see that the density gradient is first greater than 15.0 at $td = 0.0843$. This is taken as the instant when the vapor–liquid is first formed and the surface tension is first applied. As time develops to $td = 0.25$–0.50, the density becomes very steep at some section. On one side of this section, the density becomes very low, while on the other side, the density $\tilde{\rho}$ approaches 1.0. The apparent "glitch" in the density curve at $td = 0.15$ shown in Fig. 7b is, upon closer examination of the numerical printout, a reflection of a fluctuation in the density profile at nodes 7 and 8. It is caused by the introduction of the surface tension at $t = 0.0843$, since no such fluctuations are detected when no surface tension is introduced. From the physical viewpoint, the abrupt incorporation of the surface tension effects at this stage should not affect the solution because surface tension tends to zero at the critical point. Numerically, however, the instant when the critical point is first reached somewhere in the medium cannot be established with infinite accuracy; as a result, the effect of surface tension is felt suddenly rather than gradually. Fortunately, the transient abnormality disappears in a few time steps and there is no cross-over of mesh nodes in the whole calculation. Figure 7c also shows that the velocity of expansion of the vapor cavity around $td = 2.0$ is slower than that at any other time and that the expansion velocity increases for $td \geqslant 2.0$. Thus, there exists a critical radius above which the bubble expansion will accelerate. It is interesting to note that the critical bubble radius is about 0.90–1.00, occurring at $td = 2.0 \pm 0.30$. Figure 7d gives the density distribution over the range $0 < r < 12L$. The location of the vapor–liquid interface and the shock front can be readily identified.

Temperature distributions. The temperature distributions are shown in Figs. 8a, b, and c. Figure 8a is for the case of small time, i.e., $\tilde{t} \leqslant 0.280$ ($\tilde{R} \leqslant 1.74$), and is a reproduction of Fig. 9 in part I. Figures 8b and c give the temperature distributions up to the instant $\tilde{t} = 2.280$. It is clear that the temperature drops rather quickly at first, but the decrease slows down with time.

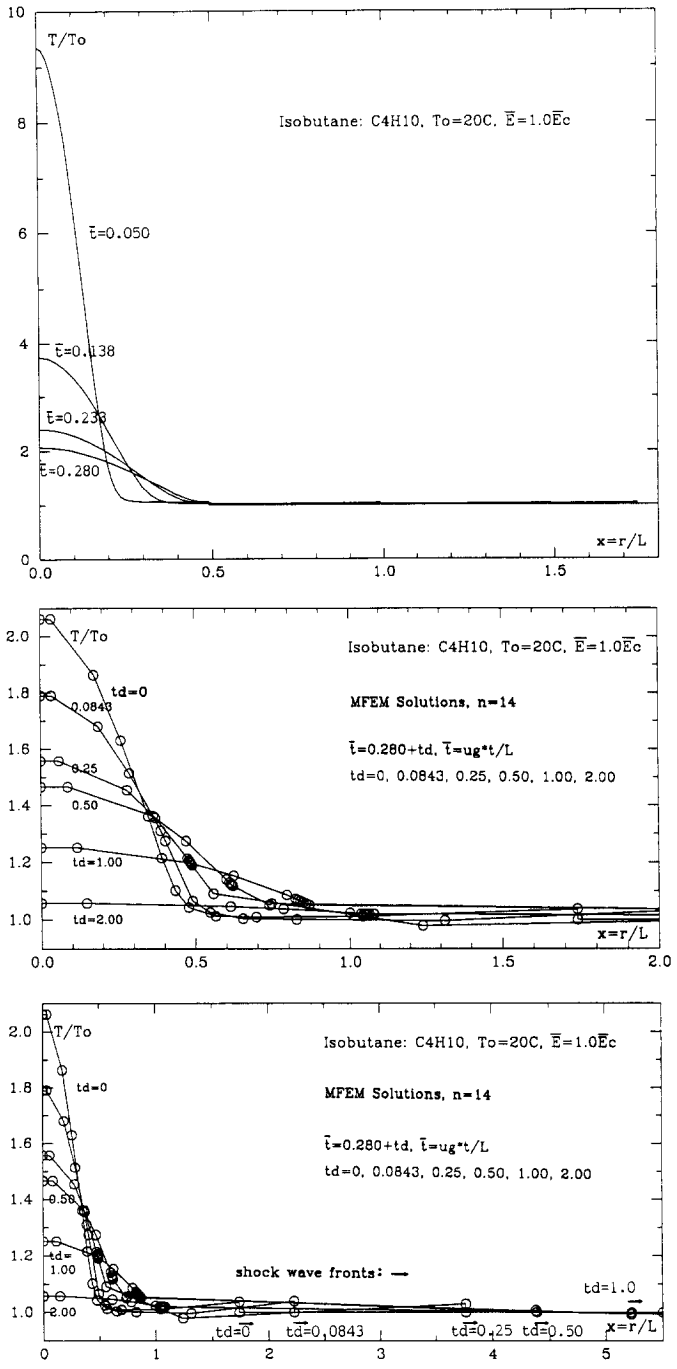

FIG. 8. Normalized temperature distributions (a) in the pre-bubble formation stage; (b) in the interface formation and developing stages from $td = 0$ to $td = 2.00$; (c) and shock waves from $td = 0$ to $td = 2.00$.

Velocity distributions. Figure 9a is a reproduction of Fig. 14 in part I with the velocity distributions for $\tilde{t} \leqslant 0.280$. Figure 9b shows the velocity distribution for $\tilde{t} > 0.280$.

6.2. *Collapse of Bubble*

The bubble will expand indefinitely in a fluid of infinite extent if the input energy is greater than the threshold

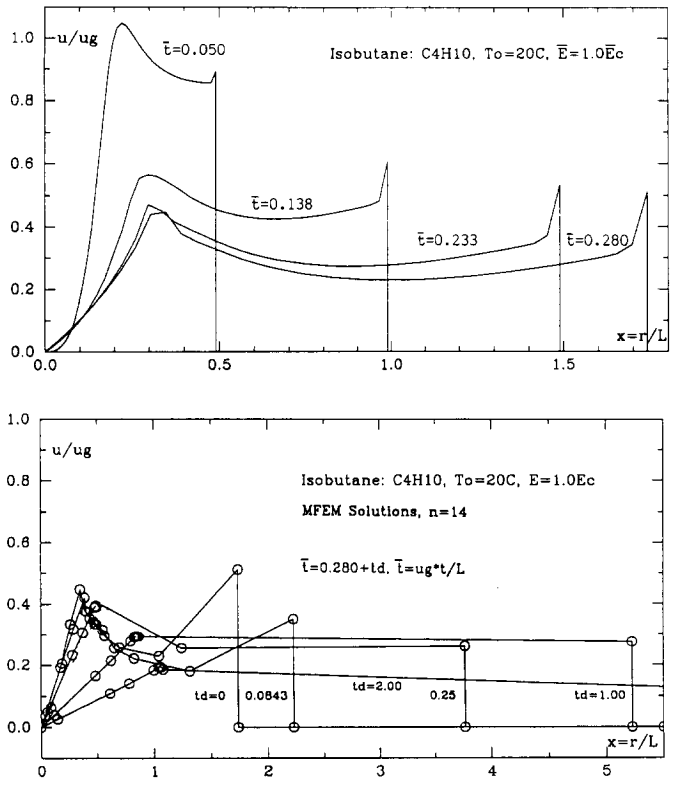

FIG. 9. Normalized velocity distributions in the (a) pre-bubble formation stage; (b) interface formation and developing stages from $td = 0$ to $td = 1.00$.

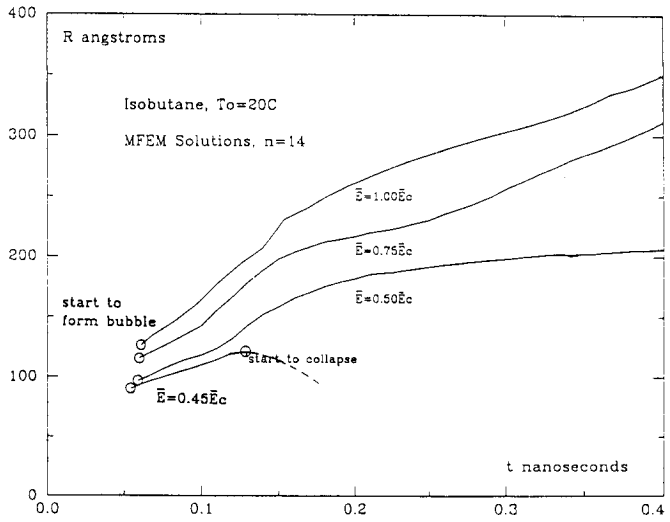

FIG. 10. Bubble radius R vs time t (isobutane).

energy; otherwise, the bubble will collapse under the action of surface tension and viscous forces. What is the collapse process? It is difficult to follow this change in the laboratory because the time scale is about 0.1–1.0 ns and the length scale is of the order of 10^2–10^3 Å. However, numerical analysis can model the actual collapse process in detail. Both isobutane with input energy $\bar{E} = 0.45(\bar{E}_c)_{\text{isobutane}}$ at $T_0 = 20°\text{C}$ and Freon-12 with input energy $\bar{E} = 0.30(\bar{E}_c)_{\text{Freon-12}}$ at $T_0 = 20°\text{C}$ are studied, where $\bar{E}_c = dE/dx$ is the experimentally determined threshold energy.

Isobutane case. The bubble will not stop expanding until approximately time $td = 1.0$ when the bubble starts to contract.

Freon-12 case. The same phenomenon occurs for Freon-12. The bubble starts to contract around $td = 2.17$ with $\bar{R} = 1.10$.

The collapse process for both isobutane and Freon-12 are shown in Figs. 10 and 11 as discussed below.

6.3. *Critical Radius and Threshold Energy*

The critical radius R_c and the threshold energy $\bar{E}_c$ can be determined by plotting R vs t, where R is the vapor radius and t is the time. Figure 10 gives the R vs t curve of isobutane. For $\bar{E} = 0.50\bar{E}_c$, $R \approx \text{const} = 200$ Å for $t \geqslant 0.20$ ns. This means that the process is almost in a state of static balance. On the other hand, if $\bar{E} = 0.45\bar{E}_c$, the bubble will start to collapse around $t = 0.13$ ns. This picture indicates that the threshold energy is $\bar{E} = 0.45\bar{E}_c$–$0.50\bar{E}_c$. The critical radius is about $R_c = 200$ Å or $R_c = 0.20 \times 10^{-5}$ cm.

Figure 11 gives the relation of R vs t for Freon-12. The bubble starts to collapse around $t = 0.08$–0.09 ns for input energy $\bar{E} = 0.30\bar{E}_c$. The threshold energy is between $0.30\bar{E}_c$ and $0.40\bar{E}_c$, and perhaps closer to $\bar{E} = 0.30\bar{E}_c$. The critical radius is about 0.90–1.05×10^{-6} cm. Table III summarizes the critical radii obtained by experiments and numerical analysis.[1]

Reviewing the above results, one finds that the comparison between the experimental and numerical results are fair, considering that a number of drastic assumptions have been made to develop a tractable model. The principal cause of the difference can be attributed to the following factors: (1) The critical radius for the spherical bubble (experimental model) is $R_c^s = 2\sigma(T)/\Delta p$, while for the cylindrical bubble (numerical model) $R_c^c = \sigma(T)/\Delta p$. This means that $R_c^s = 2R_c^c$ if surface tension σ and pressure difference Δp are the same for both cases. (2) The energy is assumed to be deposited in the media uniformly along an infinite line in the numerical analysis, while the energy in the real case is

[1] The critical bubble radii in the experiments were calculated by $R_c = 2\sigma(T)/\Delta p(T)$, where $\sigma = 13.99 - 0.1085T$ for isobutane and $\sigma = 0.1034(112 - T)$ for Freon-12. The surface tension σ for numerical solutions is determined by Eq. (44). The following are the values of surface tension calculated by above formulae at $T = 20°\text{C}$: for isobutane, $(\sigma)_{\text{numer}} = 10.89$ dynes/cm, $(\sigma)_{\text{exper}} = 11.82$ dynes/cm; for Freon-12, $(\sigma)_{\text{numer}} = 12.33$ dynes/cm, $(\sigma)_{\text{exper}} = 9.51$ dynes/cm. The ratios are $(R_c)_{\text{exper}}/(R_c)_{\text{numer}} = 5.239$ for isobutane and 5.426 for Freon-12.

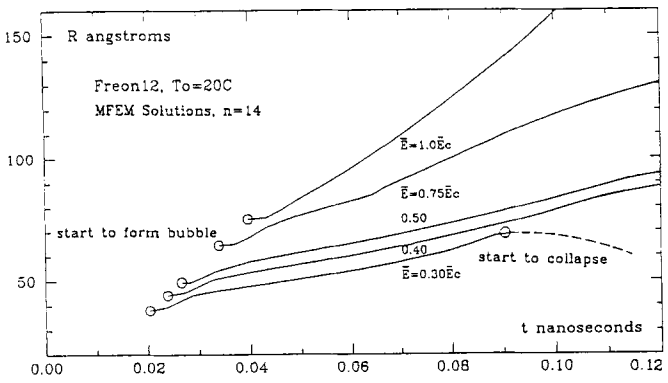

FIG. 11. Bubble radius R vs time t (Freon-12).

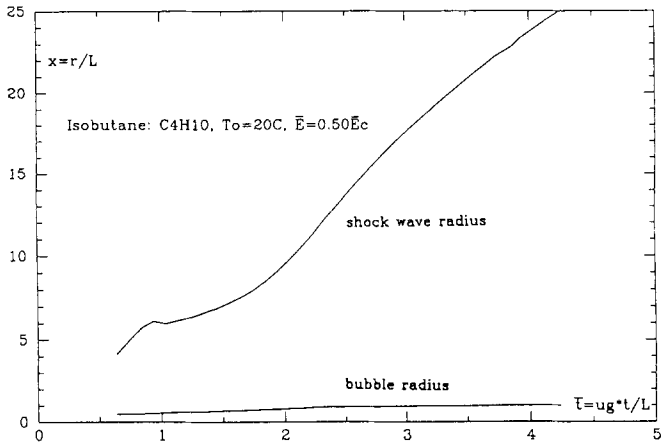

FIG. 12. Bubble radius and shock wave radius (isobutane).

deposited within a limited region. (3) The pressure difference Δp defined in experiments is given by $\Delta p = p_v - p_\infty$, where p_v is the vapor pressure within the bubble for isothermal, isobaric, and static case; and p_∞ is the pressure in the infinite region. Both p_v and p_∞ are functions of temperature T ($T = T_0 = 20°C$ in the testing cases). Therefore, the pressure difference Δp is also a function of temperature T. The above isothermal, isobaric, and static case is different from the dynamic process where the temperatures and velocities within or outside the bubble are functions of radial distance r and time t. The pressure difference Δp is always larger than that obtained by the above experimental definition. Since $\Delta p \propto 1/R_c$, one sees that although theoretical and experimental estimates of the critical radius R_c and the threshold energy are of the same order of magnitude, the theoretical values always seem to be smaller than the experimental ones.

6.4. *Shock Wave*

From the scaling transformation analysis in part I, the speed of the shock wave is given by

$$\frac{d\bar{R}}{d\bar{t}} = \frac{1}{\Gamma_0 \bar{R}}. \tag{51}$$

Integrating Eq. (51), we find

$$\bar{R} = \left(\frac{2\bar{t}}{\Gamma_0}\right)^{1/2}. \tag{52}$$

TABLE III

Numerical and Experimental Results, R_c

Item	Isobutane	Freon-12
Numerical results	0.20×10^{-5}	0.975×10^{-6}
Experimental results	1.186×10^{-5}	4.083×10^{-6}
$(R_c)_{\text{exper}}/(R_c)_{\text{numer}}$	5.930	4.188

Applying $V_s = 1/\Gamma_0 \bar{R}$ to Eq. (52), one can express the normalized shock wave speed V_s by

$$V_s = \frac{1}{\sqrt{2\Gamma_0 \bar{t}}}, \tag{53}$$

where

$$V_s = \frac{\dot{R}}{\sqrt{R^* T_0}}.$$

The above derivation can be translated as the following: The shock radius in the initial stage immediately following the sudden energy deposition increases with time as $\bar{t}^{1/2}$. The shock velocity $\dot{\bar{R}}$ varies rapidly with time as $\bar{t}^{-1/2}$.

The above relations are valid only for $\bar{R} \leqslant 0.002$. In the general case, one can draw the curves of $\tilde{R}_{\text{shock}}$ vs $\tilde{t}$ as well as $\tilde{R}_{\text{wall}}$ vs $\tilde{t}$. Figures 12 and 13 give such illustrations for isobutane and Freon-12 with input energy $\bar{E} = 0.5\bar{E}_c$ at 20°C, respectively. Figure 14 gives the shock speeds

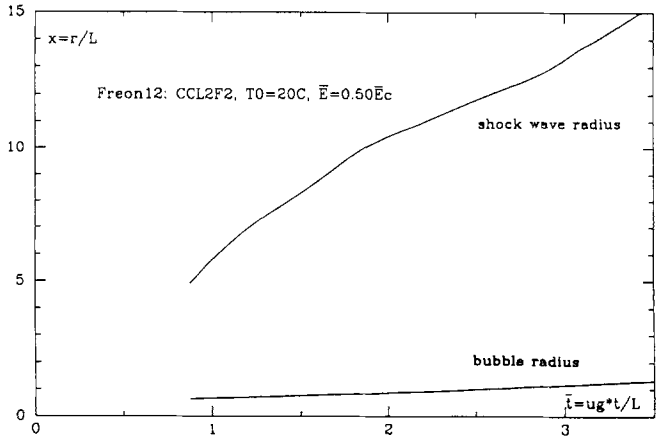

FIG. 13. Bubble radius and shock wave radius (Freon-12).

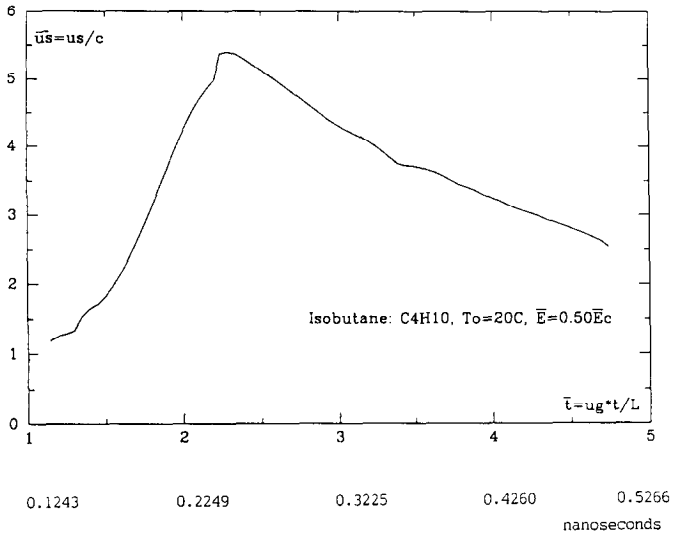

FIG. 14. Normalized speed of shock wave (isobutane).

normalized to a sound speed c of 340 m/s for isobutane with input energy $\bar{E} = 0.5\bar{E}_c$ at 20°C. The shock speeds in this case are supersonic and have a maximum around $\tilde{t} = 2.4$ and decrease later on. The speeds of the vapor–liquid interface are about 1/100 of the shock speeds.

6.5. *Some Time and Length Scales*

The time and length scales for the bubble formation depend on the given medium and the input energy. For isobutane, the bubble forms at $t = 0.05$ ns, collapses at $t =$ 0.12–0.13 ns, and the related bubble radius is about 100 Å. For Freon-12, the bubble forms at $t = 0.02$–0.04 ns, collapses at $t = 0.08$–0.09 ns, and the related bubble radius is about 50 Å. Generally speaking, the time scale for bubble formation is of the order of 10^{-2}–10^{-1} ns and for bubble collapse is of the order of 10^{-1} ns. The length scale for bubble collapse is of the order of 5×10^{1}–5×10^{2} Å. The smallness of these scales underscords the needs for numerical calculation and the difficulty of experimental measurements.

6.6. *CPU Time*

The CPU times on Micro-VAX for calculating the developing stages by using the MFEM are about $1 \sim 4$ CPU hours.

7. CONCLUSIONS AND FUTURE DIRECTIONS

7.1. *Conclusions*

The following conclusions can be presented:

(1) The general model of numerical analysis developed in this paper for solving PDE systems with initial singularity and with multiple moving steep gradients is accurate and efficient. The numerical results are in fair agreement with the experimental results. The scaling transformation and shooting technique are used to overcome the difficulty of the initial singularity, to solve the flow field of the initial stage, and to establish the initial conditions for later calculations. The implicit donor-cell finite difference method is introduced to calculate the solution for short times to improve the computational efficiency. Finally, the MFEM is successfully employed to compute the flow field in the developing stage with moving shock and moving interface. The success of solving the radiation-induced cavitation process by the above hybrid numerical model is of significance for this type of boundary value problems.

(2) The radiation-induced cavitation process can be divided into four stages. They are the initial stage, the prebubble formation stage, the interface-formation stage, and the post-interface stage. Generally speaking, the temperatures and the velocities decrease with time evolution.

(3) There is a threshold energy $\bar{E}_c$ above which the bubble will expand indefinitely and below which the bubble will collapse under the action of surface tension, viscous forces, and as well as conduction heat loss. The threshold energy and the critical radius can be obtained from the computed R vs t curves.

(4) The earlier stages of the collapse process have been calculated.

(5) The time scale for bubble formation is of the order of 10^{-2}–10^{-1} ns and the length scale of bubble radii for collapse is of the order of 5×10^{1}–5×10^{2} Å.

(6) The pressure difference Δp between the two sides of interface may be underestimated by experiments, since the average values of the pressures within the related sections for both vapor and liquid are calculated for the isothermal, isobaric and static case instead of the pressures at certain points for a dynamic case. It may lead to over-estimation of the threshold energy and the critical radius R_c.

(7) Miller's moving finite element method is found to be an efficient adaptive method which moves nodes automatically into the regions where the gradients are large. The MFEM is useful especially for solving PDE systems with multiple moving steep gradients. A general form of non-hierarchical p-version moving finite element method is derived.

7.2. *Future Directions*

Future directions may be classified into two categories:

(1) Application and improvement of the current method of solution.

(2) Extension of the current model to reflect more realistically the radiation-induced *cavitation process observed in the laboratory.*

Under the first category, one may cite the following topics for investigation:

1. Determine the threshold energy for cavitation for other types of liquid with low boiling points.
2. Study the effect of degree of superheat on the threshold energy.
3. Study the effects of viscosity, thermal conductivity, and surface tension on the solutions.
4. Modify the MFEM to handle problems with multiple propagating steep gradients. One shortcoming of Miller's method is the utilization of the regularization parameters whose values must be appropriately chosen for each type of problem studied. While Miller did indicate some of the guidelines in choosing them [8], the question remains as to whether some other scheme may be devised to overcome the difficulty of the vanishing Jacobian in the approximation matrix.

With regard to improving the current method to reflect more realistically what occurs in nature, the following topic stands out prominently: Take into account the fact that energy is deposited along a finite line rather than an infinite line as assumed in the current model. This change would require a major extension of the current program to cope with the propagation of steep gradients in three-dimensional space.

APPENDIX A

We rewrite the mass conservation equation, i.e., Eq. (22), as follows:

$$\frac{\partial \tilde{v}}{\partial \tilde{t}} = \frac{\tilde{v}^2}{\tilde{r}} \frac{\partial}{\partial \tilde{r}} \left(\frac{\tilde{u}\tilde{r}}{\tilde{v}} \right) = \frac{\tilde{u}\tilde{v}}{\tilde{r}} - \tilde{u} \frac{\partial \tilde{v}}{\partial \tilde{r}} + \tilde{v} \frac{\partial \tilde{u}}{\partial \tilde{r}}. \tag{A.1}$$

The integration of the simplest term $\tilde{u}\tilde{v}/\tilde{r}$ among them can be calculated by

$$R_1 = \left(\alpha_i, \frac{\tilde{u}\tilde{v}}{\tilde{r}} \right) = \int_{s_{i-1}}^{s_i} \frac{(x - s_{i-1})}{(s_i - s_{i-1})} \cdot \left(\frac{\tilde{u}\tilde{v}}{\tilde{r}} \right) dx + \int_{s_i}^{s_{i+1}} \frac{(s_{i+1} - x)}{(s_{i+1} - s_i)} \cdot \left(\frac{\tilde{u}\tilde{v}}{\tilde{r}} \right) dx = \lambda_1 + \lambda_2 + \lambda_3 + \lambda_4. \tag{A.2}$$

Here

$$\begin{aligned}
\lambda_1 &= (\tilde{u}_{i-1} + \zeta_m \, d\tilde{u}_{i-1})(\tilde{v}_{i-1} + \zeta_m \, d\tilde{v}_{i-1}) \, \zeta_m \times \frac{ds_{i-1}}{2} \cdot \frac{1}{(\zeta_p s_{i-1} + \zeta_m s_i)}, \\
\lambda_2 &= (\tilde{u}_{i-1} + \zeta_p \, d\tilde{u}_{i-1})(\tilde{v}_{i-1} + \zeta_p \, d\tilde{v}_{i-1}) \, \zeta_p \times \frac{ds_{i-1}}{2} \cdot \frac{1}{(\zeta_m s_{i-1} + \zeta_p s_i)}, \\
\lambda_3 &= (\tilde{u}_i + \zeta_m \, d\tilde{u}_i)(\tilde{v}_i + \zeta_m \, d\tilde{v}_i) \, \zeta_p \times \frac{ds_i}{2} \cdot \frac{1}{(\zeta_p s_i + \zeta_m s_{i+1})}, \\
\lambda_4 &= (\tilde{u}_i + \zeta_p \, d\tilde{u}_i)(\tilde{v}_i + \zeta_p \, d\tilde{v}_i) \, \zeta_m \times \frac{ds_i}{2} \cdot \frac{1}{(\zeta_m s_i + \zeta_p s_{i+1})},
\end{aligned} \tag{A.3}$$

where

$$\zeta_m = \frac{1 - 1/\sqrt{3}}{2}, \qquad \zeta_p = \frac{1 + 1/\sqrt{3}}{2},$$

$$d\tilde{u}_{i-1} = \tilde{u}_i - \tilde{u}_{i-1}, \qquad d\tilde{v}_{i-1} = \tilde{v}_i - \tilde{v}_{i-1}, \qquad ds_{i-1} = s_i - s_{i-1}$$

and

$$d\tilde{u}_i = \tilde{u}_{i+1} - \tilde{u}_i, \qquad d\tilde{v}_i = \tilde{v}_{i+1} - \tilde{v}_i, \qquad ds_i = s_{i+1} - s_i.$$

In the above derivation, the integrations are computed by

$$I(f) = f\left(-\frac{1}{\sqrt{3}} \right) + f\left(\frac{1}{\sqrt{3}} \right).$$

The corresponding terms in the Jacobian are

$$\begin{aligned}
\frac{\partial R_1}{\partial \tilde{v}_{i-1}} &= \frac{\lambda_1(1 - \zeta_m)}{(\tilde{v}_{i-1} + \zeta_m \cdot d\tilde{v}_{i-1})} + \frac{\lambda_2(1 - \zeta_p)}{(\tilde{v}_{i-1} + \zeta_p \cdot d\tilde{v}_{i-1})}, \\
\frac{\partial R_1}{\partial \tilde{u}_{i-1}} &= \frac{\lambda_1(1 - \zeta_m)}{(\tilde{u}_{i-1} + \zeta_m \cdot d\tilde{u}_{i-1})} + \frac{\lambda_2(1 - \zeta_p)}{(\tilde{u}_{i-1} + \zeta_p \cdot d\tilde{u}_{i-1})}, \\
\frac{\partial R_1}{\partial \tilde{T}_{i-1}} &= 0, \\
\frac{\partial R_1}{\partial s_{i-1}} &= -\left(\frac{\lambda_1}{ds_{i-1}} + \frac{\lambda_1 \zeta_p}{(\zeta_p s_{i-1} + \zeta_m s_i)} + \frac{\lambda_2}{ds_{i-1}} + \frac{\lambda_2 \zeta_m}{(\zeta_m s_{i-1} + \zeta_p s_i)} \right).
\end{aligned} \tag{A.4}$$

The other terms, i.e., $\partial R_1/\partial \tilde{v}_i$, $\partial R_1/\partial \tilde{u}_i$, $\partial R_1/\partial \tilde{T}_i$, $\partial R_1/\partial \tilde{s}_i$, $\partial R_1/\partial \tilde{v}_{i+1}$, $\partial R_1/\partial \tilde{u}_{i+1}$, $\partial R_1/\partial \tilde{T}_{i+1}$, and $\partial R_1/\partial s_{i+1}$ can also be derived in a similar manner.

The above sample is the simplest case for our problem. It presents a brief picture of how to calculate the Jacobian and an illustration of the enormous computational work involved.

ACKNOWLEDGMENTS

This research work has been supported in part by the U.S. Department of Energy under Contract Nos. DE-AC02-81EV10673-A000 and DE-FG02-87ER60500, and in part by the U.S. ONR under Contract No. N00014-82-K-0184. We wish to thank Professors Tony Chan, William Gropp, David Keyes, and Mitchell Smooke for their valuable discussions.

REFERENCES

1. R. E. Apfel, S. C. Roy, and Y. C. Lo, *Phys. Rev. A* **31**, 3194 (1985).
2. I. Babuska, J. Chandra, and J. E. Flaherty, *Adaptive Computational Methods for Partial Differential Equations* (SIAM, Philadelphia, 1983).
3. M. Berger, W. D. Gropp, and J. Oliger, *Numerical Grid Generation Techniques* (NASA Conference Publication, 1981), p. 2166.
4. R. J. Gelina, S. K. Doss, and K. Miller, *J. Comput. Phys.* **40**, 202 (1981).
5. C. Horvath and H. J. Lin, *Can. J. Chem. Eng.* **55**, 450 (1977).
6. J. D. Lambert, *Computational Methods in Ordinary Differential Equations* (Arrowsmith, Bristol, UK, 1973), p. 91.
7. K. Miller and R. Miller, *SIAM J. Numer. Anal.* **18**, 1019 (1981).
8. K. Miller, *Adaptive Computational Methods for Partial Differential Equations*, edited by I. Babuska, J. Chandra, and J. E. Flaherty (SIAM, Philadelphia, 1983), p. 165.
9. R. C. Reid, I. M. Prausnitz, and T. K. Sherwood, *The Properties of Gases and Liquids*, 3rd ed. (McGraw-Hill, New York, 1977).
10. M. D. Smooke and M. L. Koszykowski, *SIAM J. Sci. Statist. Comput.* 7, 301 (1986).
11. M. D. Smooke, *AIChE J.* **32**, 1233 (1986).
12. Special edition, *Comput. Methods Appl. Mech. Eng.* **55**, 1 (1986).
13. Y. Y. Sun, B. T. Chu, and R. E. Apfel, *Cavitation and Multiphase Flow Forum–50th Annu.* "ASME Conference, Cincinnati, Ohio, 1987," edited by O. Furuya, p. 45.
14. Y. Y. Sun, B. T. Chu, and R. E. Apfel, *J. Comput. Phys.* **103**, 116 (1992).
15. J. F. Thompson, *AIAA J.* **22**, 1505 (1984).